Available online at www.sciencedirect.com

ScienceDirect

journal homepage: www.elsevier.com/locate/he

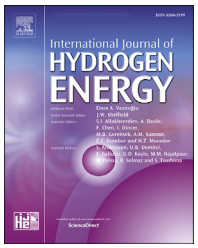

On the understanding of a cryogenic two-phase LOX/GH2 flame: Parametric sensitivity, characteristic scaling and phase instability

Yu Chen [a,b], Yu Lv [a,b,*]

[a] State Key Laboratory of Nonlinear Mechanics, Institute of Mechanics, Chinese Academy of Sciences, Beijing 100190, China

[b] School of Engineering Sciences, University of Chinese Academy of Sciences, Beijing 101408, China

HIGHLIGHTS

- Identify two distinct scalings for total heat release at lower and higher strain rates.
- Establish scalings of oxidizer vaporization rate and flame-interface distance.
- Identify the region of unstable phase in physical space and the scaling of its size.
- Find that all unstable phase states remain in the metastable region.

ARTICLE INFO

Article history:
Received 14 May 2022
Received in revised form
9 August 2022
Accepted 23 September 2022
Available online 15 October 2022

Keywords:
Cryogenic combustion
Subcritical pressure
Counterflow flame
Phase stability
Metastable region

ABSTRACT

This study concerns the cryogenic hydrogen combustion in subcritical pressure conditions, with practical relevance to rocket engine applications. A cryogenic two-phase flame in the counterflow configuration is calculated and analyzed with the consideration of real-fluid effects and heat/mass transfer across the liquid-gas interface. The effects of pressure, strain rate, fuel inlet temperature, and heat loss on the flame characteristic behaviors are examined. It is found that the vaporization rate of liquid oxidizer scales with the square-root of pressure (p) times strain rate (a_{st}), and is not a limiting factor for combustion. The total heat release scales with $\sqrt{pa_{st}}$ at lower strain rates while with $p^{4/5}a_{st}^{1/3}$ at higher strain rates. The significant results on the phase-stability of cryogenic flame are also established. It is found that the unstable phase, in terms of vapor-liquid equilibrium, arises in the vicinity of the liquid-gas interface; however, all unstable-phase states still stay in the metastable region of the phase diagram. For all the flame solutions considered in this study, no thermochemical state enters the spinodal region.

* *Corresponding author*. State Key Laboratory of Nonlinear Mechanics, Institute of Mechanics, Chinese Academy of Sciences, Beijing 100190, China.
E-mail address: lvyu@imech.ac.cn (Y. Lv).

https://doi.org/10.1016/j.ijhydene.2022.09.219

Introduction

Modern high-lift rockets [1] mostly rely on liquid-fueled rocket engines to provide thrust. Hydrogen as a high energy-density fuel has been widely adopted in the liquid-fueled rocket propulsion technology. In the liquid rocket, fuel and oxygen are carried in the liquid phase under cryogenic conditions. Cryogenic fuel and oxidizer mix and react in the combustion chamber, converting the chemical energy to thermal energy. This process is commonly referred to as cryogenic combustion. Depending on the chamber pressure, either subcritical or supercritical, previous research shows that the cryogenic combustion process exhibits distinct characteristics. At subcritical pressure, the mixing and reaction are controlled by the two-phase effects involving a series of complex physical processes, such as the liquid breakup, droplet formulation, and spray flame [2,3]. On the other hand, at supercritical pressure, the repulsive inter-molecular forces become dominant and the surface tension vanishes. It is observed that the mixing between fuel and oxidizer is more like turbulent mixing and the flame exhibits similar behaviors to gaseous flame, although the real-fluid effects, such as the existence of dense core [4] and peculiar transport properties [5], remain considerably important.

Over the years cryogenic combustion at supercritical pressures (which we will call "supercritical combustion" in the present context) has been studied extensively, and several critical understandings have been established in the literature. Through the studies in modeled configuration [6–8], it is found that the real-fluid effects of supercritical combustion are mainly pronounced near the cold oxidizer inlet. A characteristic scaling is discovered: both the flame thickness and heat release are correlated with the square root of strain rate multiplied with pressure (a slightly different scaling obtained by Huo et al. [7]). Despite the real-fluid effects on the oxidizer inlet, most of the flame region is close to the chemical equilibrium. To this end, Lacaze and Oefelein [9] assessed the suitability of the flamelet model for supercritical combustion, and they found that even with the complex thermodynamic relation and peculiar transport properties, the flamelet model remains a reasonable and robust representation of supercritical flame in diffusion-flame regime [10]. Besides, other flamelet-based modeling efforts were also carried out, including those addressing the thermodynamic aspect [11], differential diffusion effects [12], and phase-stability issue [13,14]. Since the flamelet model has been established as an effective modeling tool for supercritical combustion, it has been integrated into the CFD solver for simulating supercritical combustion in both RANS [15–18] and LES [19–24] frameworks.

In contrast to the large volume of literature on supercritical combustion, the number of studies focusing on the cryogenic combustion in subcritical pressure is limited. This is due to the fact that detailed analysis that accounts for the coupled effects of two-phase flow, heat/mass transfer (evaporation) and real-fluid thermochemistry can hardly be conducted. Therefore, the current understandings of the cryogenic combustion in subcritical pressure are gained through experimental efforts [25–31]. The general behavior of cryogenic flame in the subcritical regime is illustrated in Fig. 1. Experimental observations confirmed that the flame anchors on the injector tip. A thin flame brush is situated stably in the shear layer between the fuel and oxidizer streams, which is the major flame characteristic in the upstream/near-injector region. On the other hand, in the downstream region, the liquid jet breaks gradually into ligaments and then droplets, in which form the liquid oxidizer vaporizes into the gas phase before participating in the chemical reaction. The flame in the downstream region is characterized as a spray flame.

In this study, of our specific interest is the flame situated in the shear layer between fuel and oxidizer streams at the upstream/near-injector region, since its characteristics are crucial to the flame stabilization [28,30] and flame dynamics under thermoacoustic oscillation [32]. This peculiar stable-burning flame in the two-phase environment is facilitated by two factors. First, the high flame temperature and significant temperature gradient allow the rapid vaporization of the oxidizer so that a sufficient amount of oxidizer is released into the gas phase for reaction, which is evidenced by the very smooth surface of the liquid jet [29]. Second, the dense core of the liquid jet serves as a hydrodynamic stabilizer so that the flame is not significantly disrupted by strong turbulence or flow unsteadiness. Another remarkable aspect is that this flame configuration is similar to the counterflow configuration [33] but with an oxidizer stream in the liquid phase. This similarity provides us an avenue to study such a complex cryogenic two-phase flame under reasonable assumptions. Given the relevance and importance of cryogenic combustion to rocket propulsion, we performed a detailed computational analysis in this study to characterize a cryogenic two-phase LO_x/LH_2 flame in a counterflow setting, thereby shedding some light on the cryogenic combustion process in realistic rocket applications.

It is worth noting that Juniper et al. [34] previously carried out a study on a hydrogen counterflow diffusion flame above liquid oxygen, which has a configuration similar to the target one. However, the real-fluid effects, including non-ideal thermodynamics and particular transport properties, are not considered, and the pressure range examined in their work is too limited to reveal a robust scaling. Meanwhile, some previous studies with the focus of supercritical combustion, i.e., by Ribert et al. [6] and Huo et al. [7], also extended the analyses to the subcritical regime, but their monolithic single-phase formulation does not account for the phase interface and mass/heat transfer across it, which therefore is not suited for two-phase problems. Our computational analysis will address the above limitations by considering both the real-fluid and two-phase effects in the mathematical formulation.

In the present study, we will extend the study of Juniper et al. [34] and carry out a comprehensive analysis of the two-phase cryogenic diffusion flame in a counterflow configuration, with the consideration of complex real-fluid effects and two-phase mass/transfer effect. The objective of this study is threefold: first, we examine the flame structure and the flame behaviors in response to variations of key parameters. Second, we establish the scaling dependence of heat release, flame thickness, and flame-interface distance on the controlling parameters. Finally, we perform a single-phase stability analysis to check whether the thermochemical states in

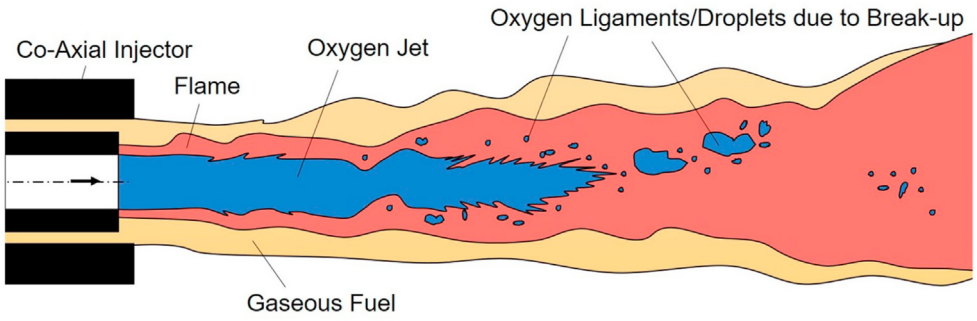

Fig. 1 – Schematic illustration of cryogenic flame in subcritical pressure (similar to the graphic illustrations in Refs. [25–28]). Note that in general fuel is preheated to gas before entering the combustor.

the combustion field satisfy the phase equilibrium. The last aspect concerns the basic assumption of our model formulation and is also a continued effort of several recent studies on the phase-stability of cryogenic flames [14,35–37].

The rest of this paper is structured as follows. We first state the problem of interest in Section 2, including the flame configuration and the specific operating conditions. Section 3 outlines the mathematical formulation of the combustion problem. In Section 4, an extensive analysis of flame structure and effects of key operating parameters will be carried out, based on which the scaling of flame characteristics with respect to pressure, strain rate, and heat loss will be presented. Section 5 concerns the phase stability of the combustion field, of direct relevance to the validity and robustness of the numerical solutions obtained in the computational analysis. The paper will be concluded by summarizing the key findings in Section 6.

Problem description and flame configuration

The flame configuration and the corresponding model problem are schematically shown in Fig. 2. As elucidated in the introduction, the cryogenic flame in the shear layer can be modeled as a two-phase counterflow flame, by setting up an interface-local reference coordinate which is traversing along the interface extension direction. In this reference frame, the liquid tangential velocity is negligible and thereby we treat the liquid as a plug flow along the interface normal direction. The liquid substance is considered to be single-component, pure oxygen and other chemical components do not diffusive into the liquid phase, because we found that other components are generally in very low concentration near the interface and their solubility in cryogenic oxygen is negligible. The fuel stream is issued from the right far field of the gas-phase domain. The liquid oxygen vaporizes first and then enters the gaseous domain to participate in the chemical reaction. The liquid-gas interface is infinitely thin and positioned at the location of $x = 0$. Across the interface, the inflow oxygen mass flux is determined via energy and component mass balances across the interface. We are interested in this particular flame in subcritical pressure conditions, and considered a range of pressure values, including 2 bar, 5 bar, 10 bar, and 30 bar. Those pressure conditions are selected to cover the whole range of subcritical conditions, from relatively low (like 2, 5 bar), to moderate (like 10 bar), to relatively high (like 30 bar)

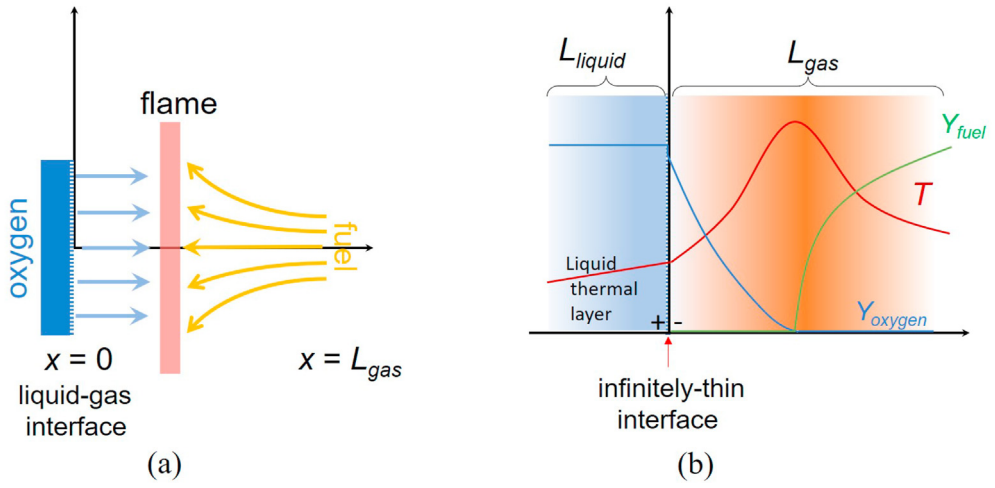

Fig. 2 – Illustration of a two-phase counterflow flame configuration (a) and the corresponding model problem (b). In (b), L_{gas} denotes the gaseous domain where combustion takes place while L_{liquid} refers to the thermal layer that could exist due to temperature gradient within liquid. "+/–" represents the left and right sides of the interface.

pressure values. Also, with a broader range of pressure conditions, the scaling relation of flame behaviors with respect to pressure can be robustly derived. The associated information about the operating conditions is provided in Table 1. The flame behaviors are characterized by examining the effects of strain rate, pressure, and fuel inlet temperature. The heat loss on the liquid side is also considered in our numerical experiment but first kept as a control variable for simplicity when investigating other physical effects.

Mathematical formulation

Governing equations

The combustion occurs in the gas-phase domain and the related physics can be described by the conservation laws of species mass, momentum, and energy. In the counterflow setting, the conservation laws can be recast into the axisymmetric forms, which are written as: for $x \in [0, L_{gas}]$,

$$G - \frac{dF}{dx} = 0, \tag{1a}$$

$$H - 2\frac{d}{dx}\left(\frac{FG}{\rho}\right) + \frac{3G^2}{\rho} + \frac{d}{dx}\left(\mu\frac{d}{dx}\left(\frac{G}{\rho}\right)\right) = 0, \tag{1b}$$

$$2F\frac{dT}{dx} - \frac{1}{c_p}\frac{d}{dx}\left(\kappa\frac{dT}{dx}\right) + \frac{\rho}{c_p}\sum_i c_{pi}Y_i\mathcal{V}_i\frac{dT}{dx} + \frac{1}{c_p}\sum_i h_i\dot{\omega}_i = 0, \tag{1c}$$

$$2F\frac{dY_i}{dx} + \frac{d}{dx}(\rho Y_i\mathcal{V}_i) - \dot{\omega}_i = 0, \tag{1d}$$

In which the functions of G, F, and H are related to radial momentum, axial momentum, and pressure as follows:

$$G(x) = -\frac{\rho v}{r}, \quad F(x) = \frac{\rho u}{2}, \quad H = \frac{1}{r}\frac{\partial P}{\partial r} \tag{2}$$

where u and v are the axial and radial velocity components; ρ, T and P are the density, temperature, and pressure. c_p is the heat capacity at constant pressure, κ and μ are the thermal conductivity and dynamic viscosity, respectively. The mass diffusion velocity is expressed as [38]:

$$\mathcal{V}_i = \frac{1}{X_i\overline{W}}\sum_j W_j D_{ij}\frac{dX_j}{dx} - \frac{D_i^T}{\rho Y_i T}\frac{dT}{dx}, \tag{3}$$

where Y_i and X_i are the mass fraction and mole fraction of ith species, respectively. W denotes the molecular weight, D_{ij} and D_i^T refer to the binary and thermal diffusion coefficients, respectively. The liquid stream is treated as a plug flow of pure liquid oxygen, and its governing equation reads: for $x \in [-L_{liquid}, 0]$,

$$\frac{d}{dx}(\rho_l u_l) = 0, \tag{4a}$$

$$\rho_l u_l c_{p,l}\frac{dT_l}{dx} - \frac{d}{dx}\left(\kappa_l\frac{dT_l}{dx}\right) = 0, \tag{4b}$$

With the subscript "l" to indicate the liquid variable. Note that without further specification other variables without the subscript "l" represent the gas-phase quantities.

At the far field of the fuel stream, the inlet temperature and velocity (zero radial component) are prescribed. At the infinitely-thin liquid-gas interface ($x = 0$), the phase change process is taking place. It is assumed that the phase change at the interface occurs very fast and the equilibrium condition prevails. In general, the interface temperature depends on the oxygen boiling temperature and the partial pressure of oxygen vapor on the gas side of the interface, for instance, according to the Clausius Clapeyron relation. However, it is found that the phase change of our problem turns out to be indeed sufficiently fast and the oxygen concentration dominates on the gas side of the interface (later we will show $Y_{O_2} > 98\%$ at $x = 0^-$ in our cases). Hence, the interface temperature is approximated as the boiling temperature of liquid oxygen $T(x = 0) \approx T_{O_2,sat}$, at a given pressure. Note that this approximation was employed in modeling droplet combustion and found in the classical literature [39,40]. Furthermore, the oxidizer supply is governed by the heat and mass flux balances across the interface. The inflow mass flux of liquid oxygen, denoted as $\dot{m}_o$, is determined from the energy conservation law (from the '+' side to the '-' side) [39]:

$$\dot{m}_o\Delta h_{vap} + \left(\kappa\frac{dT}{dx}\right)\Big|_{l^+} = \left(\kappa\frac{dT}{dx}\right)\Big|_{g^-}, \tag{5}$$

where the first and second terms on the left-hand side refer to the latent heat and heat conduction towards the liquid side, and the term on the right-hand side is the heat conduction from the gaseous side. Since the vaporized species is pure oxygen, $\dot{m}_o$ is also the oxygen mass flux across the interface. Therefore, the interface naturally enforces the boundary condition for the oxygen transport equation in gas phase, which is written as [39]:

$$\dot{m}_o = \rho u Y_{O2} + \rho Y_{O2}\mathcal{V}_{O2}, \tag{6}$$

Meanwhile, because the liquid is always treated as pure oxygen, at the interface ($x = 0$), the zero-mass-flux boundary condition is motivated for other species,

$$0 = \rho u Y_i + \rho Y_i\mathcal{V}_i, \quad \text{with } i \neq i_{O2}. \tag{7}$$

It should be noted that Eqs. (5)–(7) are coupled with each other. Another interesting aspect is that when the liquid is fixed at the boiling temperature, we have $(\kappa dT/dx)|_{l^+} = 0$ and we may solely sove the governing equations of the reactive gas mixture, Eq. (1). In the present work, we employed a modified version of FlameMaster [41] to solve the nonlinear ODE system. The solver is based on an iterative Newton method with the Jacobian matrix evaluated numerically with

Table 1 – Operating pressures and the corresponding parameters for the cryogenic flame analysis.

Pressure (bar)	Saturation Temperature (K)	Latent heat (kJ)	Liquid thermal Conductivity (W/K)
2	97.4	204.86	0.1413
5	109.0	191.08	0.1243
10	120.0	174.01	0.1080
30	142.0	115.25	0.0746

divided differences. To account for the liquid-gas interface, we extended the solver's capability by including the heat- and mass-relations, Eqs. (5)–(7). To ensure the numerical convergence, we continually increase numerical resolution until the solution does not change. Typically, each flame is resolved by about 400 grid points with an extremely dense grid near the oxidizer side. We carried out and reported the validation study with comparison to DNS data in Ref. [14]. More validation efforts can be found in Appendix. A.

Models of thermodynamics, transport, and chemistry

To account for the real-fluid thermodynamics, a cubic equation of state (EoS) must be employed and we select the Peng-Robinson EoS [42] because of its simplicity and demonstrated accuracy in the previous studies. For mixtures, the EOS is expressed as follows:

$$P = \frac{\mathcal{R}T}{v-b} - \frac{a(T)}{v^2+2bv-b^2}, \tag{8a}$$

$$a = \sum_i \sum_j X_i X_j a_{ij} \quad \text{and} \quad b = \sum_i X_i b_i, \tag{8b}$$

$$a_{ij} = 0.45724 \frac{\mathcal{R}^2 T_{c,ij}^2}{P_{c,ij}} \left(1 + c\left(1 - \sqrt{\frac{T}{T_{c,ij}}}\right)\right)^2, \tag{8c}$$

$$b_i = 0.07780 \frac{\mathcal{R}T_{c,i}}{P_{c,i}}, \tag{8d}$$

$$c_{ij} = 0.37464 + 1.54226\omega_{ij} - 0.26992\omega_{ij}^2, \tag{8e}$$

In which $\mathcal{R}$ is the universal gas constant, $v = 1/\rho$ is the specific volume, ω is the molecular acentric factor, and T_c and P_c denote the critical temperature and pressure, respectively. Note that the mixing rule recommended by Harstad et al. [43] is utilized here. The binary critical properties are evaluated with:

$$T_{c,ij} = \sqrt{T_{c,i}T_{c,j}}(1 - k_{ij}), \tag{9a}$$

$$P_{c,ij} = Z_{c,ij}\mathcal{R}T_{c,ij}/v_{c,ij}, \tag{9b}$$

$$v_{c,ij} = \left(v_{c,i}^{1/3} + v_{c,j}^{1/3}\right)^3 \Big/ 8, \tag{9c}$$

$$Z_{c,ij} = (Z_{c,i} + Z_{c,j})/2, \tag{9d}$$

$$\omega_{ij} = (\omega_i + \omega_j)/2, \tag{9e}$$

where v_c is the critical molar volume, Z_c is the critical compressibility factor and k_{ij} is the binary interaction parameter.

Besides, in order to evaluate the heat capacity and enthalpy of the real-fluid mixture in Eq. (1), we follow the standard procedure [44,45]. The mixture properties at the standard ideal-gas state are first evaluated with the NASA polynomial [46], and then the real-fluid properties are obtained by adding a correction (often called departure function) to the corresponding ideal-gas properties. To accurately capture the real-fluid effect, the peculiar diffusive transport behavior of real fluids must be taken into account. In this regard, Chung et al.'s formulations [47] are employed to evaluate viscosity and thermal conductivity, and the formulations reduce to the classical Chapman-Enskog equations [48] at low pressure. In terms of diffusivity evaluation, the semi-empirical method proposed by Takahashi [49] is used, in which the real-fluid diffusivity (scaled by the corresponding ideal-gas value) is expressed as a function of a pair of reduced pressure and temperature. In the present study, we focus on hydrogen-oxygen combustion, and the chemical kinetics is described by Burke et al.'s chemical kinetics [50], including 9 species and 27 elementary steps. We selected Burke et al.'s chemical Kinetics mechanism because it is a well-validated hydrogen reaction mechanism applicable to a large range of pressure conditions, which has been broadly employed in related studies [13,14,36,51]. The critical properties of all species are taken from the NIST database [52]. It is noted that there is a lack of experimental data for several minor species; however, the mass of these minor species only accounts for less than 1% of the overall mass of the reactive mixture. This issue is treated using a pragmatic approach in which the minor species without critical-property data are eliminated from the EoS-related calculations and their enthalpy and heat capacity properties revert to the corresponding values of ideal gases.

Analysis I: characteritization of flame behaviors

Flame structure

Fig. 3(a) shows the structure of the two-phase cryogenic flame in a one-dimensional counterflow setting. The flame temperature is very high due to the high heating value of hydrogen. There is a significant temperature gradient near the interface, which is in the order of 10^6 K/m (for the case of $a_{st-} = 100\ s^{-1}$). However, due to the large magnitude of latent heat, the oxygen inflow velocity is still very slow compared to that of the fuel inflow. Two peaks in the heat-release profiles are observed, corresponding to fuel-rich and fuel-lean mixtures, respectively, which coincide with the two local strain extrema. The same behavior was also found in the previous studies of supercritical flames [53,54]. Further, it is worth noting that the oxygen mass fraction at the interface is not restrictively (although very close to) unity. This is because the boundary conditions of the species transport equations at the liquid-gas interface (x = 0) are not Dirichlet conditions. Instead, the species mass fractions at the interface are determined by a set of coupled relations (Eqs. (3), (5) and (6)) that describe the heat and mass transfer across the liquid-gas interface. As a result, the oxygen concentration exhibits a small jump at the interface. Nevertheless, the jump is very small. In our cases, the oxygen mass fraction at the interface is above 98%

Fig. 3(b) and (c) show the comparison of flame structures at two different strain rates, $a_{st} = 100\ s^{-1}$ (near-equilibrium) and $a_{st} = 3.70 \times 10^6\ s^{-1}$ (extinction strain rate, a_{ex}). Since the species concentration at the oxidizer inlet varies with respect to the strain rate, the comparison was carried out on the space of

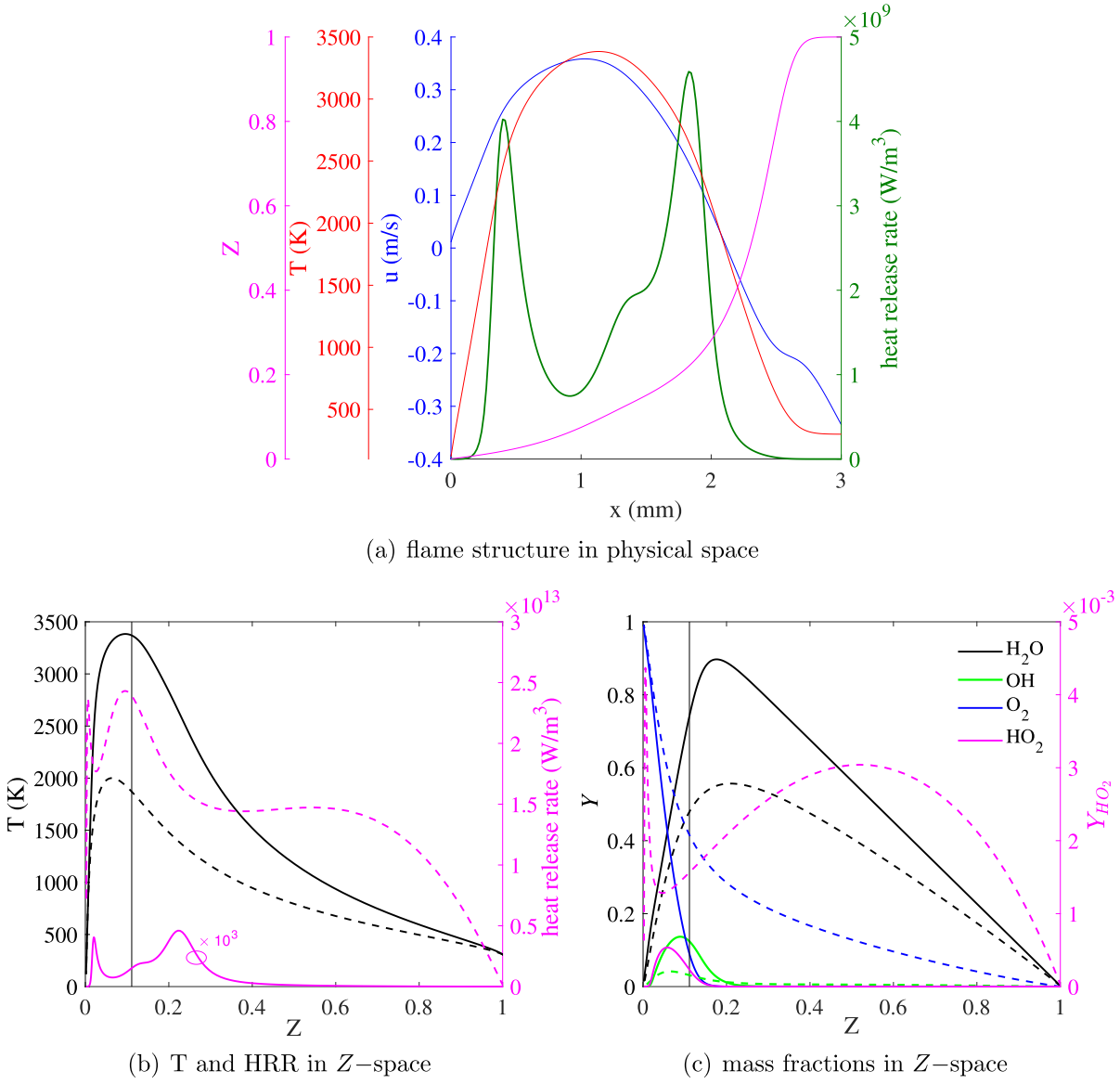

(a) flame structure in physical space

(b) T and HRR in $Z-$space

(c) mass fractions in $Z-$space

Fig. 3 – Structure of counterflow cryogenic GH_2/LO_2 flame at the 10 bar pressure and a strain rate of $a_{st} = 100\ s^{-1}$ (a) and comparisons of the profiles of flame temperature and heat release rate (b) and species mass fractions (c) at two different strain rates: $a_{st} = 100\ s^{-1}$ (solid line) and $a_{st} = a_{ex}$ (dashed line). The curve of heat release rate in panel (b) is multiplied by a factor of 1000 to be visible.

mixture fraction, defined using hydrogen element mass in the mixture,

$$Z_H = W_H\left(\frac{Y_H}{W_H} + 2\frac{Y_{H_2}}{W_{H_2}} + 2\frac{Y_{H_2O}}{W_{H_2O}} + \frac{Y_{OH}}{W_{OH}} + \frac{Y_{HO_2}}{W_{HO_2}} + 2\frac{Y_{H_2O_2}}{W_{H_2O_2}}\right). \quad (10)$$

The peak temperature is located at $Z_H = 0.097$ smaller than $Z_H = 0.111$, the value corresponding to stoichiometry for the pure-oxygen/hydrogen case. This is attributed to the effect of differential diffusion as also observed in the results in Yao et al. [36]. The influence of differential diffusion is more pronounced at higher strain rate, while the flame temperature peak moves closer to the oxidizer inlet. Interestingly, at the extinction strain rate ($a_{st} = a_{ex}$) the two heat-release-rate peaks are both positioned on the fuel-lean side, and the one originally on the fuel-rich side is very close to the stoichiometry. To better examine the differential diffusion effect, we follow the procedure of Sutherland et al. [55] to evaluate a differential diffusion parameter, which is defined as:

$$\epsilon = \sum_{\ell=1}^{N_e} \gamma_\ell \epsilon_\ell, \quad \epsilon_\ell \equiv -\sum_{i=1}^{N_s} \frac{a_{\ell i} W_\ell}{W_i} \mathcal{V}_i - \nabla\cdot\left(\rho D \nabla\left(\sum_{i=1}^{N_s} \frac{a_{\ell i} W_\ell}{W_i} Y_i\right)\right) \quad (11)$$

where N_e and N_s are the numbers of elements and species, respectively. $a_{\ell i}$ is the number of atoms of the element l in species i. γ_ℓ denotes the weighting factors of the elements in the definition of the mixture fraction [55]. We plot the normalized differential diffusion parameters of the given flames in Fig. 4. As shown, the differential diffusion is very

significant on the fuel side due to the high diffusivity of the hydrogen molecules. This result is consistent with Yao et al.'s finding [36] in the supercritical conditions. Moreover, they also found that the differential diffusion parameter can be intensified across the pseudo-boiling line, which is exemplified as a localized sharp peak. Since here we considered subcritical condition and the evaporation does not occur on the gaseous domain, therefore that sharp feature does not exist in our cases.

As exhibited in Fig. 3, the species concentrations also show strong sensitivities to the strain rate. At low strain rate condition, there is only marginal oxygen leakage towards the fuel-rich side; when strain rate achieves the quenching point, the oxygen leakage becomes significant and the mass fraction of major product-water reduces by nearly 40%. Coincidence with the oxygen leakage is the continuous reduction of OH concentration with the growth of strain rate. OH, as one of the most active radicals, is mostly distributed around the location of peak temperature. Note the good correlation between the OH and the temperature profiles in Fig. 3 (b) and (c). At a higher strain rate, OH drifts towards the cold oxidizer side to sustain the required heat release, meanwhile, a lower temperature environment impedes the production of OH. This leads to a much lower level of OH concentration. Another remarkable behavior due to the strain rate variation is the accumulation of inactive HO_2 radical at the quenching condition, which is attributed to the intensified recombination reaction at the lower temperature level [40]. In contrast to the localized distribution of HO2 radical at a low strain rate, the HO2 at the high strain rate becomes widespread in the entire Z − space due to the significant diffusion effect. In the vicinity of the interface where the temperature is very low, a spike appears in the HO_2 mass-fraction profile, which results from the very lower temperature near the liquid-gas interface. Such a peculiar feature of HO2 was not reported previously in the classical counterflow flame setting [7]. Although there are some notable changes in the thermochemical states close to the interface, the variation of oxygen mass fraction at the interface is less than one percent from $a_{st} = 100\ s^{-1}$ to $a_{st} = a_{ex}$.

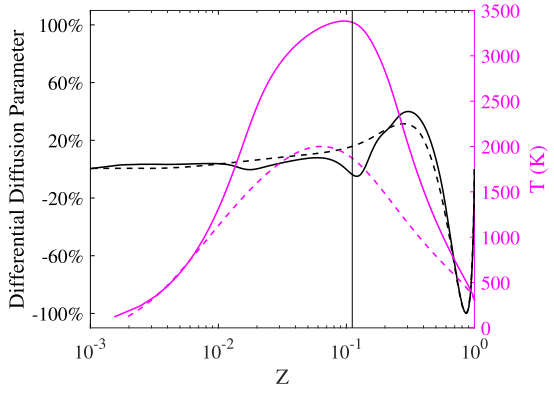

Fig. 4 − Differential diffusion parameter ϵ profiles corresponding to the counterflow cryogenic GH2/LO2 flame at two strain rates in Fig. 3.

Effects of pressure and strain rate

In this part, we examine the effects of pressure and strain on the flame characteristics simultaneously. Fig. 5(a) shows the peak flame temperature as a function of stoichiometric strain rate, a_{st}. Similar to the results established for supercritical flames, the flame temperature is not receptive to strain rate in low strain-rate conditions, because of the oxy-combustion environment and highly reactive fuel (hydrogen). The flame temperature starts dropping when a_{st} becomes larger than approximately 1% of its extinction value—a_{ex}. The continuous growth of a_{st} finally leads to a considerable drop in the flame temperature. Based on this behavior, we may categorize the flame behaviors into two regimes: i) a lower strain-rate regime, $a_{st} \leq 1\% a_{ex}$, and ii) a higher strain-rate regime, $a_{st} > 1\% a_{ex}$. To quantify the flame behaviors in response to different physical effects, in the following we focus the analysis on three characteristic variables: (i) total heat release, $\dot{Q} = \int_0^L \sum_i h_i \omega_i dx$, (ii) flame-interface distance, δ_{FI}, defined as the spatial distance between the interface and the locus of peak flame temperature, and (iii) the vaporization rate of liquid oxygen, $\dot{m}_o$ (see Eq. (5)).

It is interesting to see that the total heat release exhibits different behaviors in the two regimes defined above, as shown in Fig. 5(b). In the lower strain-rate regime, the total heat release scales with strain rate and pressure as $\dot{Q} \sim \sqrt{p a_{st}}$, which is consistent with the finding in Juniper et al.'s study [31] and the results for supercritical flames [6,8]. However, in the high strain-rate regime, the scaling of total heat release shifts to a different form, $\dot{Q} \sim p^{4/5} a_{st}^{1/3}$ for the flame we considered. The change in scaling is attributed to the fact that flame temperature responds differently to strain rate in different regimes. Temperature drop at higher strain rates leads to a relatively weakened heat release. The latter scaling was not identified previously since not enough operating conditions were considered. Apart from the scaling about total heat release, the scaling for the flame-interface distance, δ_{FI} and the vaporization rate of liquid oxygen, $\dot{m}_o$, are also established: $\delta_{FI} \sim 1/\sqrt{(p a_{st})}$ and $\dot{m}_o \sim \sqrt{p a_{st}}$, as illustrated in Fig. 5(c) and (d), respectively. For each of the two scalings, its form is kept consistent in two regimes, throughout the entire range of flammable strain rates. We can also compare the scaling of $\dot{m}_o$ in Fig. 5(d) to that of $\dot{Q}$ in Fig. 5(b). As the strain rate approaches the quenching point, the oxidizer vaporization rate tends to grow faster than the total heat release, comparatively speaking, with respect to the strain rate. Hence, this indicates that the flame quenching is caused by the overwhelming diffusive straining effect, and not a result of the lack of oxidizer supply from the liquid phase. This significant finding is directly relevant to the stabilization of cryogenic flame in the actual combustion chamber and is also supported by the experimental evidence (i.e., the stable reaction zone in the shear layer [28,30,31] and the smooth surface [29]). These experimental evidences corroborate our finding that for the cryogenic flame configuration considered here, the oxidizer supply from the liquid phase is not the limiting factor for combustion.

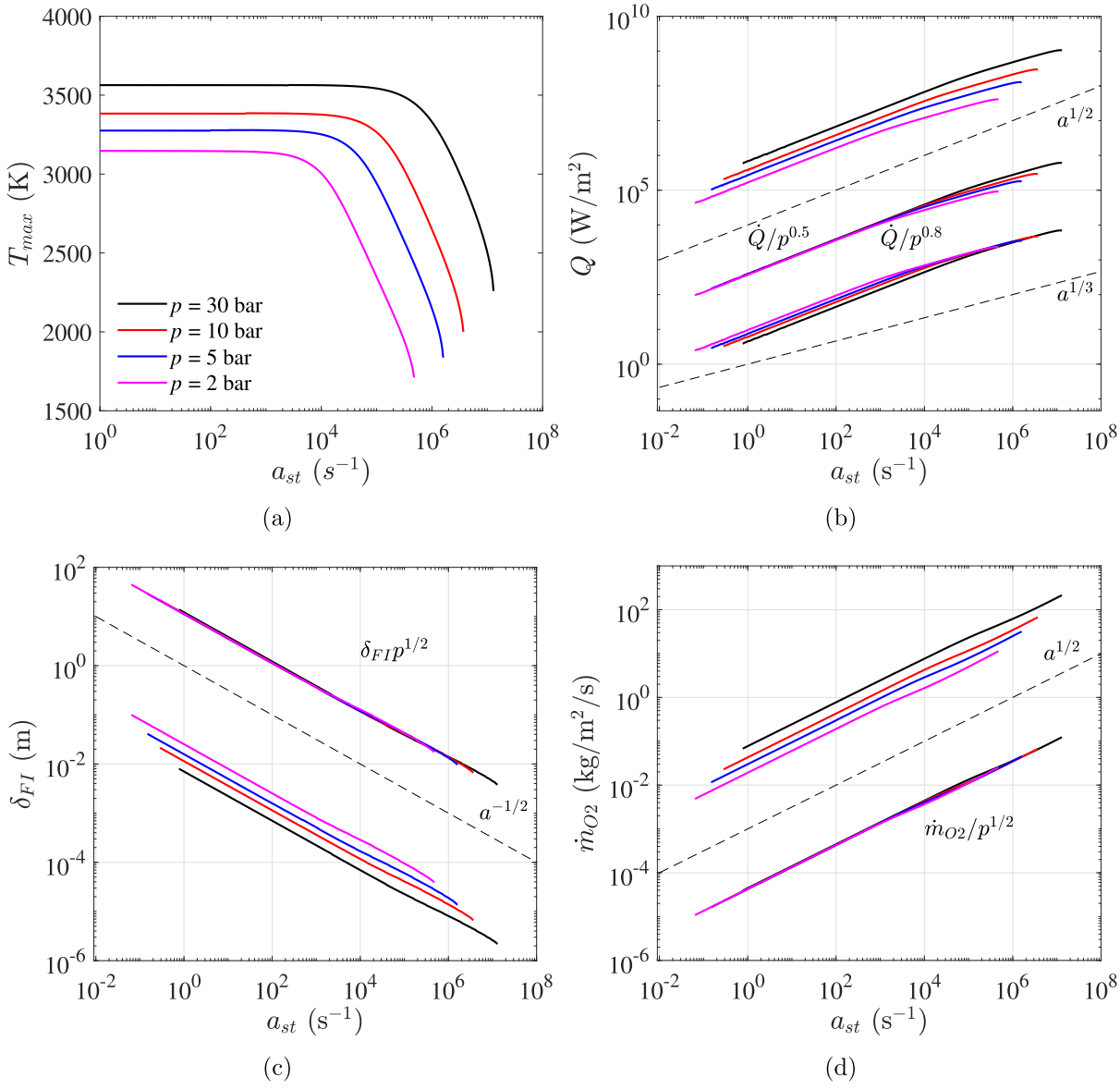

Fig. 5 – Effects of pressure and strain rate on the (a) peak flame temperature; (b) total heat release, $\dot{Q}$; (c) flame-interface distance, δ_{FI}; and (d) vaporization rate of oxidizer, $\dot{m}_o$.

Effect of real fluid

It is known that close to the interface the temperature is very low and the real-fluid effect might play a vital role in combustion. The effect of real fluid is investigated in the mixture fraction in Fig. 6. As shown, the compressibility factor (defined as $PV/\mathcal{R}T$) deviates from unity as the mixture fraction Z_H approaches zero. Specifically, the non-ideal thermodynamic effect is pronounced when $Z_H < 4 \times 10^{-3}$. This range of mixture fraction is generally consistent with the finding for supercritical counterflow flame [9]. With increasing operating pressure, the compressibility factor near the interface becomes smaller, and hence the non-ideal effect is growing. The direct impact of real fluid is well illustrated in the density profile in Fig. 6(b). As we can see, the density obtained based on the ideal gas law can introduce significant model errors, especially for the intermediate pressure range. At $P = 30$ bar, the error in density is almost 100%. Below $P = 2$ bar, the model error is bounded within 7%. Since the density is tied to the mass and heat transfer between two phases, these errors directly result in the errors in oxidizer inflow velocity and the species concentration. Therefore, the real-fluid effect should be accounted for in the modeling of cryogenic flames, especially when the operating pressure is close to the critical point.

Effect of fuel inlet temperature

The fuel inlet temperature is found to play a minor role in the behavior of two-phase cryogenic flame, which is similar to the finding for supercritical flames [7,9]. Here we select three inlet temperatures, namely 300 K, 500 K, and 700 K, based on practical relevance, to examine this effect. Compared to the oxygen inlet temperature, the fuel inlet temperature is generally higher as in rocket applications the fuel undergoes a

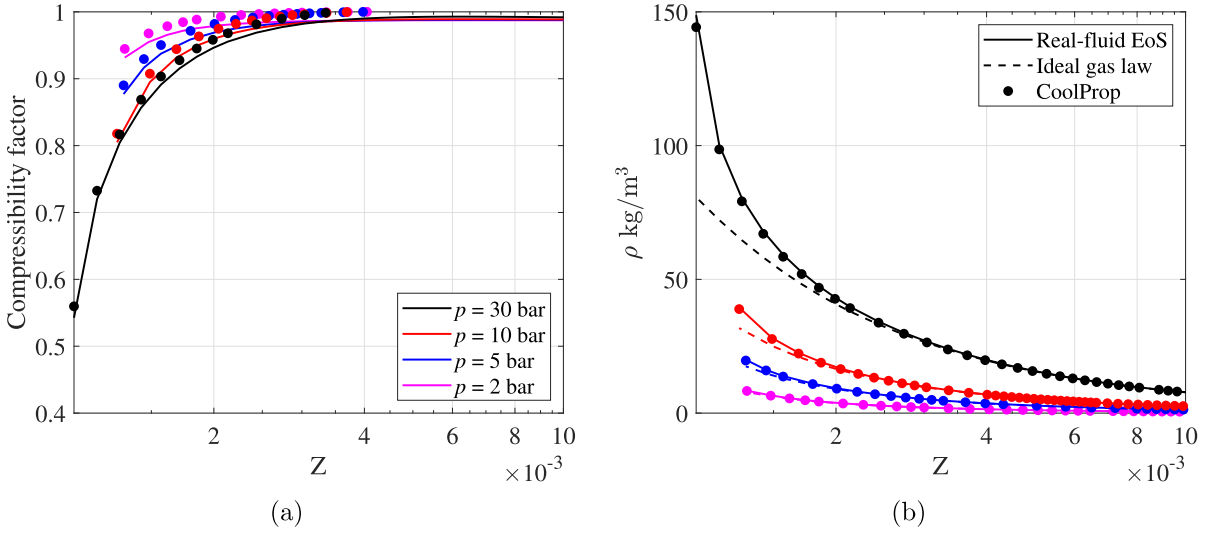

Fig. 6 – Profiles of (a) compressibility factor and (b) density in the mixture-fraction space for different pressure conditions. In (b) the results obtained with the ideal-gas law are shown in dashed lines. Data in (a) and (b) are compared against the reference data from CoolProp [56] at given (T, p, Y_i) conditions.

reburning process before being injected into the combustion chamber. As shown in Fig. 7, the change of fuel inlet temperature causes a minimal change in the flame characteristics. The small change in flame temperature can be explained by the classical theory of diffusion flame [40]. The adiabatic flame temperature is related to the fuel inlet temperature as:

$$\Delta T_{max} \approx Z_{st} \Delta T_f, \tag{12}$$

where the stoichiometric mixture fraction Z_{st} may be replaced by $Z|_{T=T_{max}}$ for our case due to the differential diffusion effect. As discussed in Sec. 4, $Z|_{T=T_{max}}$ is about 0.097 in our case. Hence, it is expected that the 200 K increase in fuel inlet temperature corresponds to about 19 K rise in peak flame temperature, which coincides with the results in Fig. 7. The consistency between the predictive and theoretical analyses in this regard implies that the non-ideal gas effects in the considered flame are not as pronounced as those in the high-pressure conditions [9]. The slight sharpening of the temperature profile near the interface also leads to a marginal increase in oxygen vaporization rate. Nevertheless, the flame characteristics are not sensitive to fuel inlet temperature, and this is also corroborated with the results in Fig. 7 (b), where the extinction strain rates for different fuel inlet temperatures are nearly the same. Finally, we should note that the slight sensitivity of the flame to fuel inlet temperature is due to the fact that i) Z_{st} here in Eq. (12) is very small and ii) the highly reactive flame overshadows the real-fluid effect and exhibits similar features as a Burke-Schumann flame. Caution should be taken when

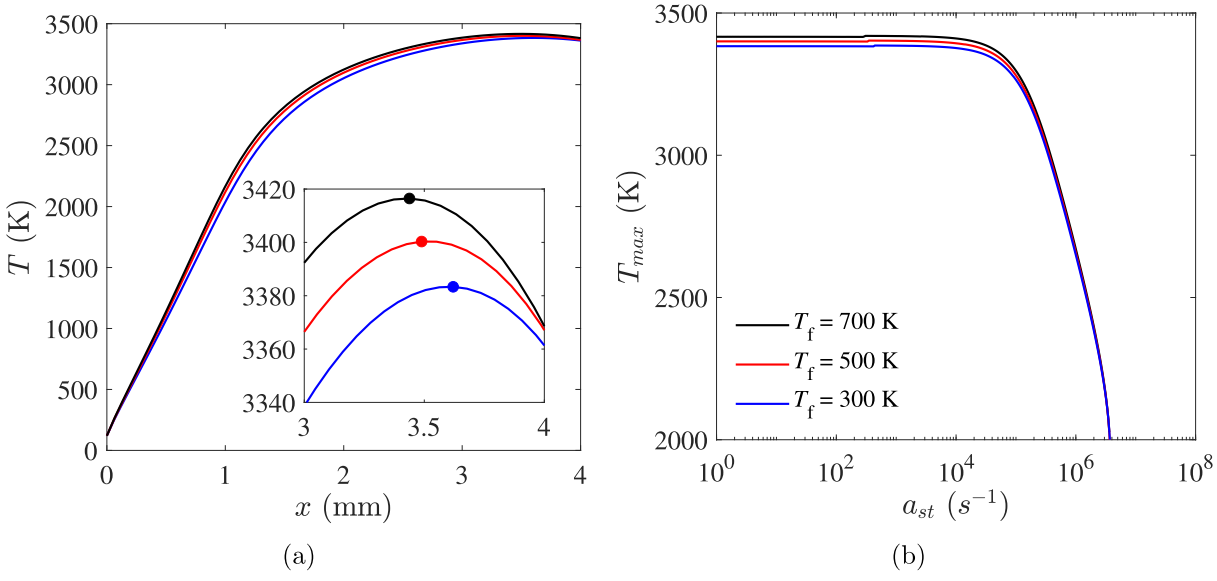

Fig. 7 – Behavior of cryogenic counterflow LO2/GH2 flame in response to the change of fuel inlet temperature at 10 bar pressure. (a) temperature profile; and (b) peak temperature versus strain rate.

generalizing this observation to other fuel types and flame conditions.

Effect of heat loss to liquid

In the above analysis, the heat conduction towards the liquid side is not considered and the bulk liquid is fixed at the saturated temperature to reduce the number of control variables. To account for the non-zero heat flux toward the oxygen liquid, we need to resolve the liquid temperature within the thermal layer adjacent to the liquid-gas interface. To this end, we would like to find the practically-relevant parameters. In rocket-relevant applications, the size of the thermal layer may be compared to the size of the injector (See Fig. 1). Since the injector diameter is typically in the order of millimeter, we consider the thickness of the thermal layer, L_{liquid}, to be $\mathcal{O}(0.1)$ millimeter or even smaller. The temperature of the bulk liquid could be lower than the boiling temperature by $\mathcal{O}(10)$ K. In general, these parametric ranges are rather reliable for rocket combustion. With the ranges of parameters, we solve the plug-flow transport equations, Eq. (4), to obtain the temperature profile in the liquid as well as the liquid heat flux at the interface. Since this heat flux represents extra heat loss from the gas side in Eq. (5), we denote it as $\dot{Q}_{loss} = (\kappa dT/dx)|_{l^+}$ in the following for notational convenience. Fig. 8(a) shows the temperature profile in the liquid region with various thermal layer thicknesses and with a bulk liquid temperature of 80 K at the pressure of $p = 10$ bar. As shown, the temperature exhibits a linear profile within the thermal layer at all cases. The temperature profile becomes steeper as the thermal layer narrows down, which implies much larger heat loss to the liquid from the interface. In 8(b), the $\dot{Q}_{loss}$ is plotted against the thermal layer thickness L_{liquid}. An exponential growth of $\dot{Q}_{loss}$ is observed with the decrease of L_{liquid}.

With this set of $\dot{Q}_{loss}$ values, we then carry out the counterflow flame calculation in the gas phase to examine the effect of $\dot{Q}_{loss}$ on flame characteristics. The results are shown in Fig. 9. With a growing $\dot{Q}_{loss}$, the flame becomes closer to the interface, and the temperature profile there is sharpened; however, simultaneously the liquid vaporization rate reduces and the oxygen concentration on the interface decreases, leading to lower flame temperature and lower overall heat release. The continuous growth of heat loss causes flame extinction eventually, similar to the influence of strain rate. The effect of heat loss may be contrasted against that of strain rate, as summarized in Table 2. The peak flame temperature and flame-interface distance are negatively correlated with both heat loss and strain rate. Moreover, total heat release and oxidizer vaporization rate are negatively correlated with heat loss, while positively correlated with strain rate. In addition, the interfacial oxygen concentration exhibits negative correction with heat loss but is insensitive to the strain rate. Finally, it is also worth noting that major flame characteristic quantities have a linear dependence on heat loss, but are proportional to the square root of strain rate.

As elucidated at the beginning of this section, we choose the problem setting based on the practical scenario of relevance to rocket combustion. The heat loss to the liquid side is directly related to the thickness of the thermal layer that appears close to the injector of the rocket combustor. In general, the thermal layer size could be $\mathcal{O}(0.1)$ millimeters. As such, it is shown here that the heat loss to liquid could have an appreciable influence on the characteristics of the two-phase flame but is unlikely to cause flame extinction. Note that the extreme case considered here has a thermal-layer thickness of $'.'\infty$ millimeter, which is difficult to persist in practical settings. This conclusion is also consistent with the analysis of Juniper et al. [34].

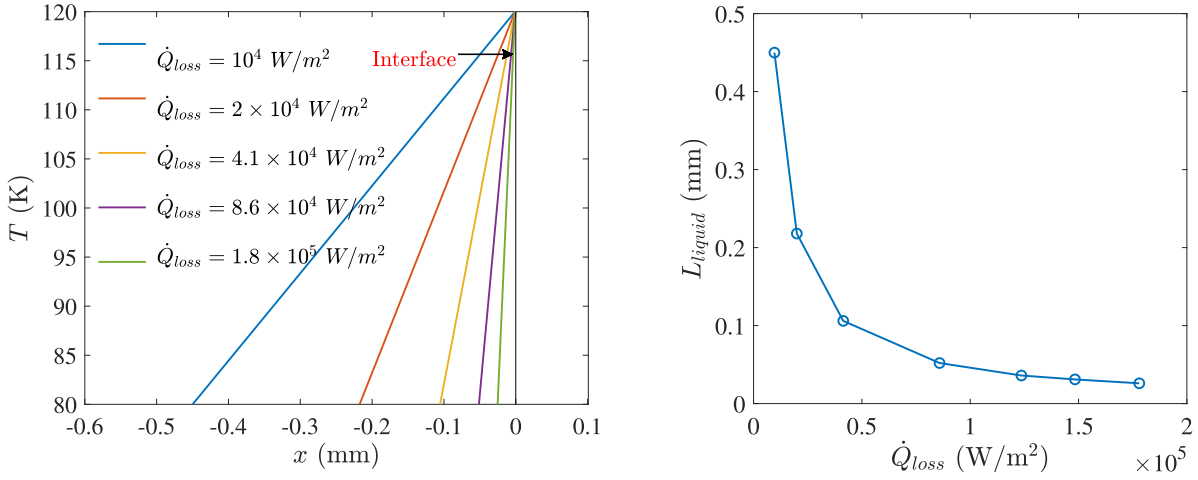

(a) temperature profile (b) heat flux vs. thermal-layer size

Fig. 8 – Plug flow solution in the liquid region with various thermal layer thickness: (a) temperature profile; (b) relation between the thermal layer thickness and the heat flux at the interface. The legend in (a) illustrates the heat flux resulting from different cases.

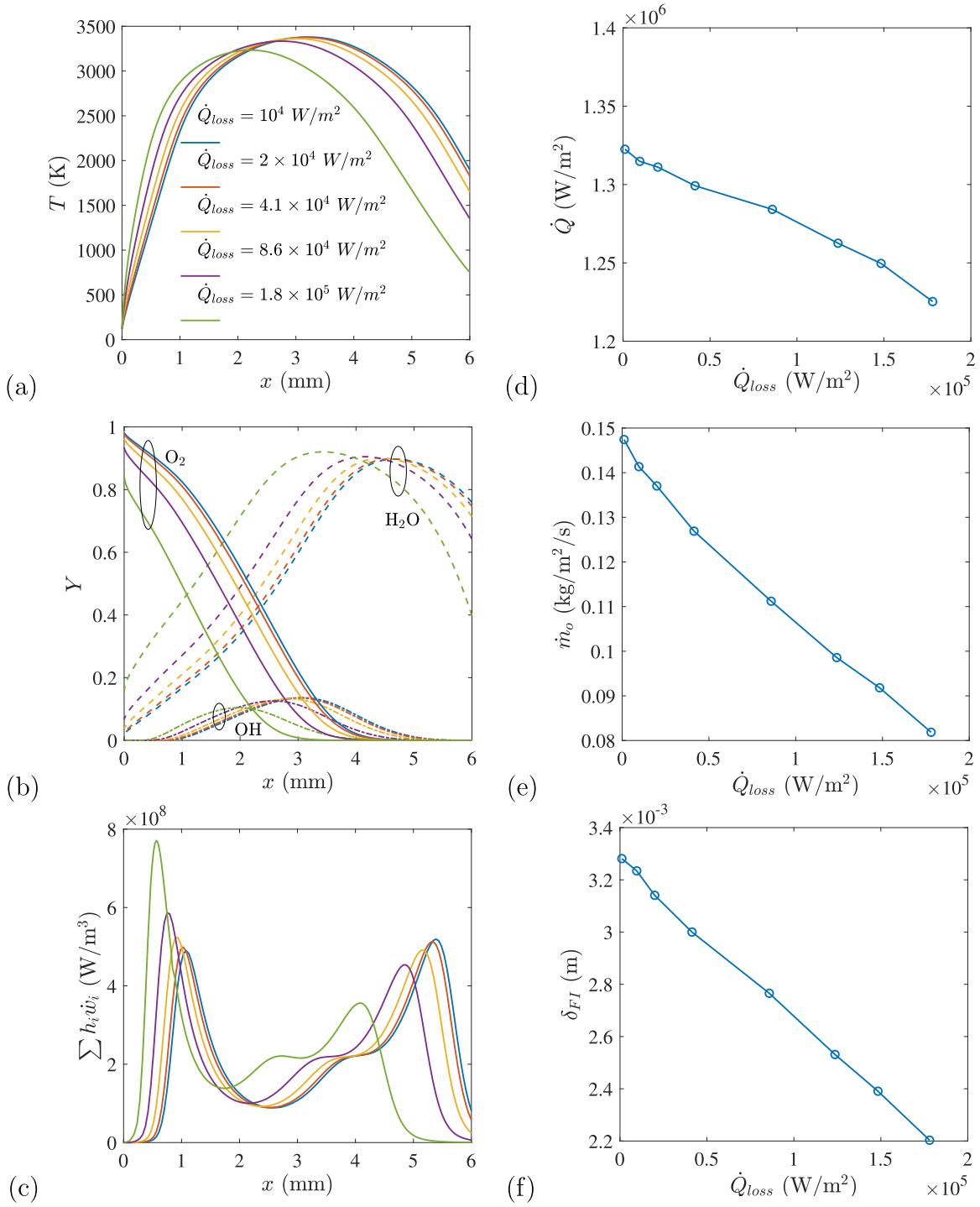

Fig. 9 – Effect of heat loss to liquid on the cryogenic counterflow LO2/GH2 flame at the 10 bar pressure and a fixed strain rate. (a), (b) and (c) panels, respectively, show the profiles of temperature, heat release rate and species mass fraction; (d), (e) and (f) panels, respectively, reveal the behaviors of flame-interface distance, liquid-oxygen vaporization rate and overall heat release.

Analysis II: a posteriori analysis of phase stability

Phase stability of the cryogenic flame is another primary focus of our study because phase stability is critical to model applicability and fidelity. Previous studies have identified the presence of unstable phase in supercritical combustion field [14,35,36]. However, the phase stability of cryogenic flame in the subcritical regime has not been investigated yet. To rigorously analyze this problem, we follow the approach of Traxinger et al. [35] and examine phase stability from two

Table 2 – Comparison of the effects of heat loss and strain rate on the flame characteristics.

Flame characteristics	Heat loss $\dot{Q}_{loss}$	Strain rate a_{st}
Peak flame temperature	Negatively correlated	Negatively correlated
Flame-interface distance	Negatively correlated	Negatively correlated
Total heat release	Negatively correlated	Positively correlated
Oxidizer vaporization rate	Negatively correlated	Positively correlated
Interfacial oxygen concentration	Negatively correlated	Insensitive

perspectives: vapor-liquid equilibrium (VLE) and metastability. For VLE, the criterion based on tangent plane distance (TPD) proposed by Michelsen [57] is utilized in a posterior manner to examine whether a single-phase (gaseous) mixture stays at its lowest Gibbs energy state. Herein a yes-or-no answer will first be provided; however, the phase instability identified through VLE does not mean that the phase separation is necessarily triggered, as the thermodynamic state could lie in a metastable state. The metastable region represents the area between the binodal and spinodal curves in the phase diagram. In the metastable state, any small disturbance to the state is unlikely to result in phase separation. Therefore, additional investigation is conducted to examine the metastability of the thermochemical states on each flame manifold.

Phase stability with VLE

Previous studies [14,35,36] shown that an unstable phase appears in the region of lower temperature and with appreciable water concentration. In the following, we refer to this region as the unstable-phase region (UPR). The same finding holds true in this present study, as the VLE unstable phase emerges in the narrow region adjacent to the liquid-gas interface. In Fig. 10, we show that the boundary of UPR collapses well with the iso-contour lines of $T = 300$ K and $X_{H2O} = 4\%$. In other words, the unstable phase likely arises when the temperature is lower than 300 K and the local water volume fraction stays above 4%. Such a thermochemical environment commonly exists very close to the liquid-oxygen stream in rocket combustors. This value of $X_{H2O} = 4\%$ also provides us a rapid estimate of the upper bound of the vapor fraction of the two-phase mixture in case that phase separation occurs locally.

Based on the scaling behavior of the flame-interface distance (δ_{FI}) shown in Sec. 4.2, we expect that overall topology scales of the flame inversely with the square root of strain rate, and thus the same scaling holds for the size of UPR. These characteristics are well illustrated in Figs. 10 and 11(a). In addition, Fig. 11(a) also shows the scaling of the size of UPR, δ_{UPR}, with respect to pressure. Below 10 bar pressure, UPR shrinks with increasing pressure, and δ_{UPR} scales inversely with the square root of pressure. This scaling behavior with respect to pressure is consistent with that of δ_{FI} revealed in Fig. 5(c). However, remarkably the UPR size no longer reduces as pressure further elevates. This peculiar characteristic behavior implies that the existence of an unstable phase is a persistent feature at a higher pressure range (even in the supercritical regime). Fig. 11(b) shows the relative size of UPR with respect to the flame-interface distance. As we can see, except for a slight increase near the quenching point, the relative size of UPR is almost constant over the range of flammable strain rate. Furthermore, the relative size of UPR is insensitive to pressure variation below 10 bar, but thereafter exhibits a significant growth with rising pressure, indicating a considerable broadening of the UPR (relative to the flame thickness) at high pressure conditions. Overall, the size of UPR is very small compared to the flame-interface distance (less than 5% of δ_{FI} for all cases considered), which implies a significant challenge and resolution requirement for modeling purposes if one would like to capture the unstable phase in CFD simulations.

Phase metastability

In this part, we focus on the metastability of the obtained flame solutions. This requires the determination of the metastable regions, which, however, is rather difficult and impractical for multi-component mixtures. Since it is known that the controlling factors on phase stability are mainly temperature and water concentration based on the VLE analysis, hence we use the metastable region of H_2O/O_2 binary mixture manifested in the $T - X_{H2O}$ plane for reference to examine the metastability of the flame solutions. The procedure is following: first, the binodal and spinodal lines of the H_2O/O_2 binary mixture are obtained for a given pressure and plotted in the $T - X_{H2O}$ plane (the region in between these two lines is the metastable region); then, each flame solution at the corresponding pressure is laid on top of the same plot to reveal the loci of its thermochemical states with respect to the metastable region.

Fig. 12 shows the loci of the thermochemical states on each flame manifold in the $T - X_{H2O}$ plane, along with the corresponding metastable region, for different pressure conditions. It is evident that only the thermochemical states very close to the liquid oxygen lie within the metastable region, and for a given flame case the state closest to the spinodal curve corresponds to the very thermochemical state of the liquid-gas interface. In our analysis, the most important finding is that no state is located within the spinodal region where phase separation inevitably occurs, meaning that the thermochemical states of all flame solutions considered in this study are either stable or metastable. Pressure has an impact on the size of the metastable region but does not change the metastability of the flame solutions. With descending pressure, the temperature levels of both coexistence and spinodal lines fall while the metastable region is somewhat expanded and the distances between the loci of metastable flame states and the spinodal region become larger. The strain rate also plays a role in the metastability of the cryogenic flame. As discussed in Sec. 4, the higher strain rate reduces the water concentration

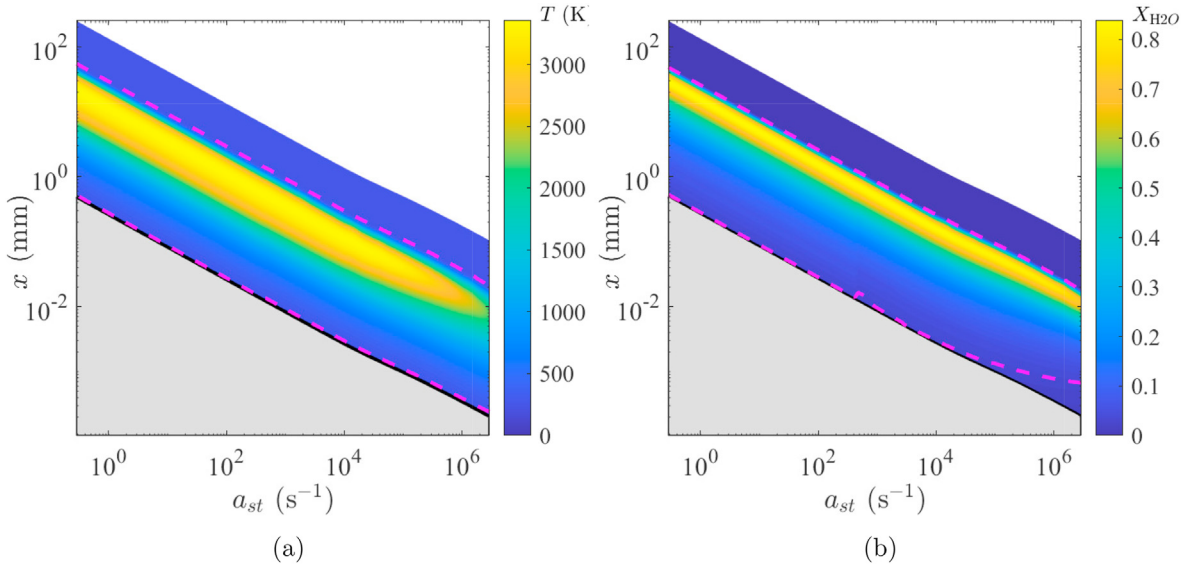

Fig. 10 – Locations of unstable-phase region in the cryogenic LO_x/GH_2 flames subjected to various strain rates. The UPR is shown as the gray zone, laid on top of the temperature profile (a) and the water concentration profile (b). The dashed pink lines in (a) and (b) correspond to the iso-contour lines of 300 K and $X_{H2O} = 4\%$, respectively. The operating pressure is 10 bar.

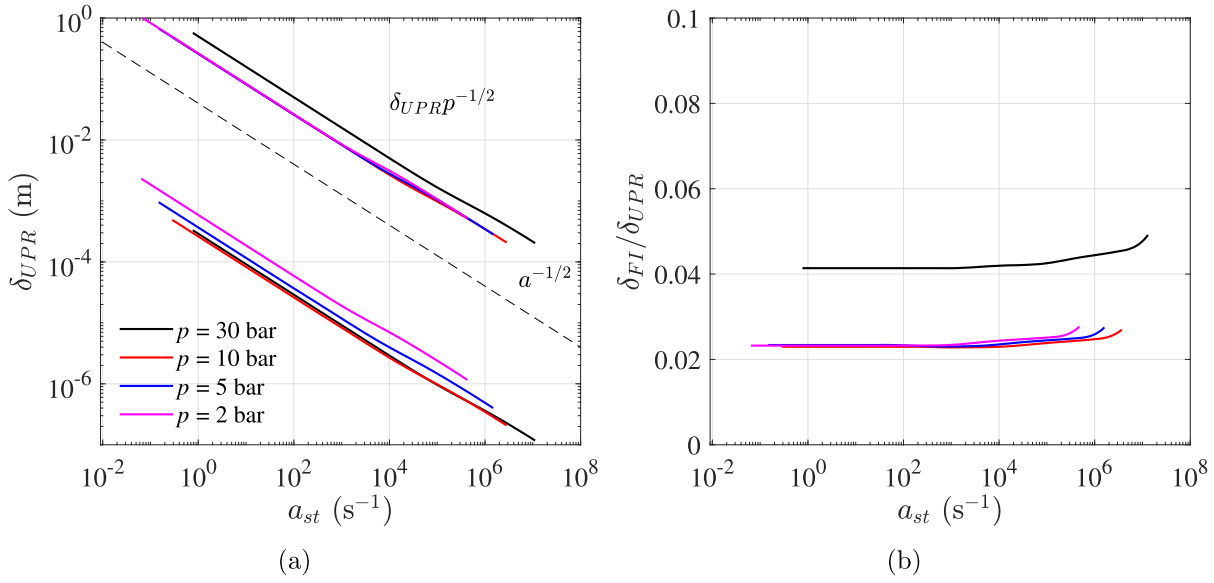

Fig. 11 – Size and relative size of the unstable-phase region of the cryogenic LO_x/GH_2 flame under different pressure and strain-rate conditions. Shown in (a) are the size of UPR and its scalings and in (b) is the size of UPR relative to the flame-interface distance.

in the vicinity of the liquid-gas interface, leading to the left move of thermochemical states in the T-X_{H2O} plane. In fact, this interesting finding is a bit counter-intuitive, saying that a highly-strained flame is less likely to encounter phase separation issues compared to a flame with a lower strain rate. Overall, here our analysis on metastability considers a range of pressure and strain-rate conditions, which is an appreciable extension of the study by Traxinger et al. [35]. Moreover, we also carry out a tentative analysis on the nucleation process, which is possibly triggered in the metastable phase by appreciable thermodynamic disturbance events. Based on the classical nucleation theory [58], it is found that the water droplets form immediately in the metastable phase when the pressure is above 5 bar; while at the 2 bar condition the nucleation time scale is in order of 100 s. The readers are referred to the Appendix. B for more details.

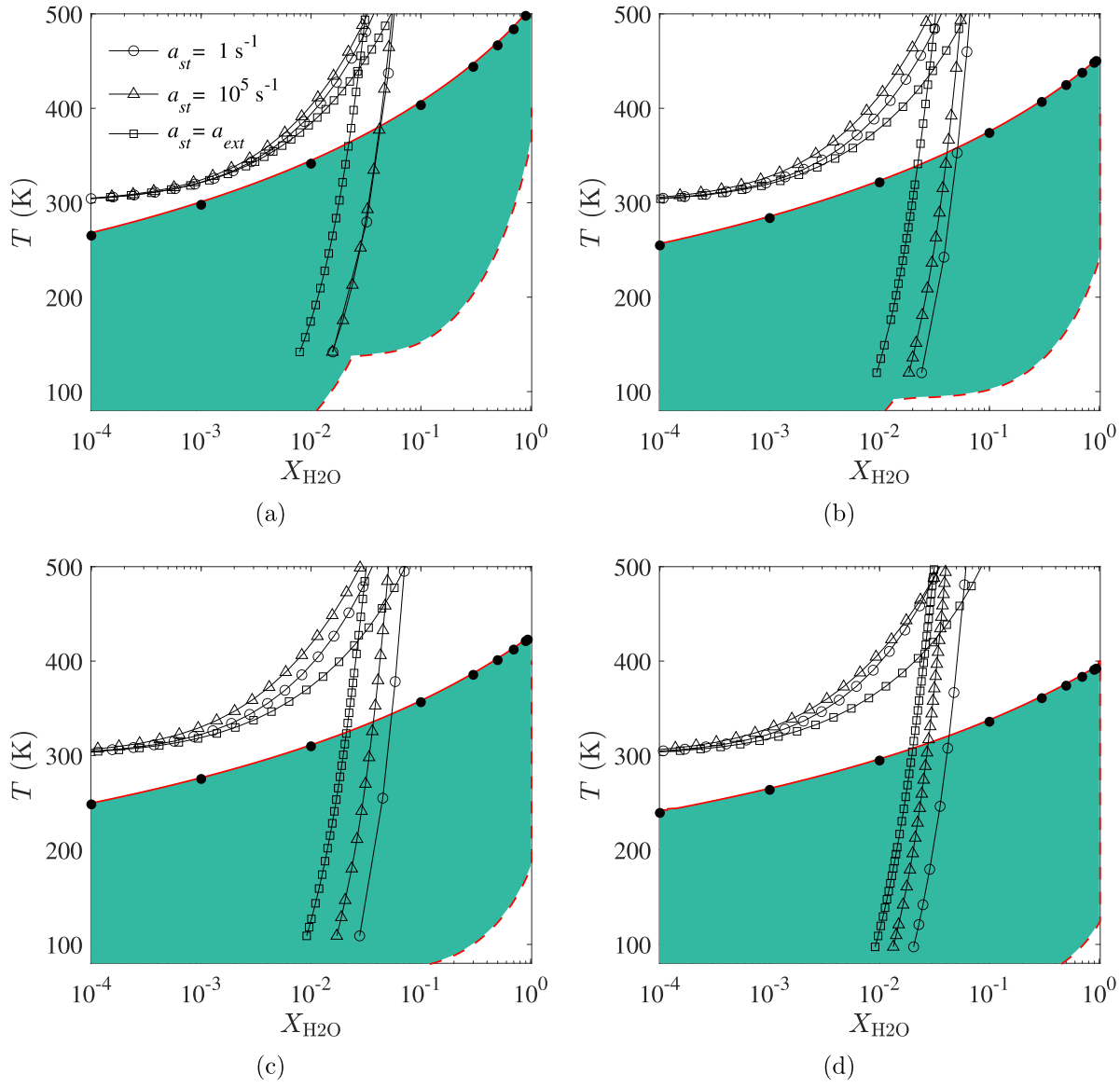

Fig. 12 – Loci of the thermochemical states on each flame manifold in the $T - X_{H2O}$ plane and the metastable regions under various pressure conditions: (a) 30 bar, (b) 10 bar, (c) 5 bar and (d) 2 bar. The green-colored zones represent the metastable regions of the H_2O/O_2 binary mixture at different pressures. The solid and dashed lines in red correspond to the binodal and spinodal lines. The dots denote the reference data obtained from CoolProp [56]. (For interpretation of the references to colour in this figure legend, the reader is referred to the Web version of this article.)

Conclusions

A counterflow cryogenic LO_x/GH_2 flame was characterized through computational analysis. The particular focus was placed on the flame behaviors at subcritical pressures, which have not been studied thoroughly. The real-fluid thermodynamic and transport models, along with the detailed chemical mechanism, were incorporated into the model formulation, and importantly the heat-transfer and mass-transfer across the liquid-gas interface were accounted for. A parametric study was carried out to examine the impacts of a number of influencing factors (pressure, strain rate, fuel inlet temperature, etc.) on flame behaviors. In addition, the phase stability analysis was performed to determine whether the thermochemical states on flame are in phase equilibrium or positioned in the metastable thermodynamic region. Our study leads to several key findings, which are summarized as follows.

- Scalings of flame characteristic variables, including total heat release, flame-interface distance, and oxidizer vaporization rate were established. It is found that the scaling of total heat release varies with the magnitude of strain rate. The scaling, $\dot{Q} \sim \sqrt{pa_{st}}$, holds well in lower strain rates at which flame temperature is not receptible to strain rate, while in the higher strain-rate range where the flame temperature becomes sensitive to strain rate, the

scaling shifts to $\dot{Q} \sim p^{4/5} a_{st}^{1/3}$. It is recognized that the flame-interface distance scales with pressure and strain rate as $\delta_{FI} \sim 1/\sqrt{pa_{st}}$, and the scaling of oxidizer vaporization rate is found to be $\dot{m}_o \sim \sqrt{pa_{st}}$. These two scaling rules are not influenced by the magnitude of strain rate and hold firmly throughout the entire range of flammable strain rates. By comparing the scalings of $\dot{Q}$ and $\dot{m}_o$, we also confirmed that the oxidizer supply through liquid vaporization is not a limiting factor for the cryogenic flame considered.

- Our study shows that the real-fluid effects are pronounced only in the vicinity of the liquid-gas interface (mixture fraction less than 4×10^{-3}) and become increasingly crucial as pressure approaches the critical point. The effect of fuel inlet temperature was also investigated and found to have a very limited influence on flame characteristics.
- A new finding in our study is that the heat loss to the liquid oxidizer can have a profound impact on the flame characteristics. With growing heat loss, the total heat release, the flame-interface distance, and the oxidizer vaporization rate all exhibit linear decreasing trends. Moreover, when the heat loss becomes sufficiently high, a considerable drop of oxygen concentration at the interface is observed.
- Another substantial result is about the phase-stability of cryogenic flames. Based on the vapor-liquid equilibrium theory, we find that the unstable phase appears in the vicinity of the liquid-gas interface. The size of the unstable-phase region scales with the square root of strain rate reduces with increasing pressure and stabilizes when pressure approaches the critical value. Additional investigation on the metastability of the unstable phase was performed. It is confirmed that the thermodynamically unstable phase are all situated in the metastable region where small disturbances in the thermochemical state will not trigger phase separation.

Declaration of competing interest

The authors declare that they have no known competing financial interests or personal relationships that could have appeared to influence the work reported in this paper.

Acknowledgement

This work is supported by the NSFC Basic Science Center Program for “Multiscale Problems in Nonlinear Mechanics” (No. 11988102). YL acknowledges the startup support from the Chinese Academy of Sciences. We thank Zheng Qiao and Lu Chen for many helpful discussions.

Appendix A. Supplementary data

Supplementary data to this article can be found online at https://doi.org/10.1016/j.ijhydene.2022.09.219.

REFERENCES

[1] Mao H, Li Y, Wang L, Xie F, Wang J. Investigation on the difference of geyser behaviors among different cryogenic fuels of launch vehicle. Int J Hydrogen Energy 2020;45(58):34150–62.
[2] Gai G, Kudriakov S, Rogg B, Hadjadj A, Studer E, Thomine O. Numerical study on laminar flame velocity of hydrogen-air combustion under water spray effects. Int J Hydrogen Energy 2019;44(31):17015–29.
[3] Gadalla M, Kannan J, Tekgül B, Karimkashi S, Kaario O, Vuorinen V. Large-eddy simulation of tri-fuel combustion: diesel spray assisted ignition of methanol-hydrogen blends. Int J Hydrogen Energy 2021;46(41):21687–703.
[4] Mayer W, Telaar J, Branam R, Schneider G, Hussong J. Raman measurements of cryogenic injection at supercritical pressure. Heat Mass Tran 2003;39(8–9):709–19.
[5] Okong’o NA, Bellan J. Direct numerical simulation of a transitional supercritical binary mixing layer: heptane and nitrogen. J Fluid Mech 2002;464:1–34.
[6] Ribert G, Zong N, Yang V, Pons L, Darabiha N, Candel S. Counterflow diffusion flames of general fluids: oxygen/hydrogen mixtures. Combust Flame 2008;154(3):319–30.
[7] Huo H, Wang X, Yang V. A general study of counterflow diffusion flames at subcritical and supercritical conditions: oxygen/hydrogen mixtures. Combust Flame 2014;161(12):3040–50.
[8] Juanós AJ, Sirignano WA. Pressure effects on real-gas laminar counterflow. Combust Flame 2017;181:54–70.
[9] Lacaze G, Oefelein JC. A non-premixed combustion model based on flame structure analysis at supercritical pressures. Combust Flame 2012;159(6):2087–103. https://doi.org/10.1016/j.combustflame.2012.02.003.
[10] Cao W, Zhou Z, Zhou W, Xu S, Xiao Q, Cao W, Jiao F, Zhang Y, Yu S, Xu S. The flow field behaviours of under-expansion jet flame in premixed hydrogen/air explosion venting. Int J Hydrogen Energy 2022;47(18):10420–30.
[11] Kim S-K, Choi H-S, Kim Y. Thermodynamic modeling based on a generalized cubic equation of state for kerosene/LOx rocket combustion. Combust Flame 2012;159(3):1351–65.
[12] Kim T, Kim Y, Kim S-K. Numerical analysis of gaseous hydrogen/liquid oxygen flamelet at supercritical pressures. Int J Hydrogen Energy 2011;36(10):6303–16.
[13] Banuti DT, Ma PC, Hickey J-P, Ihme M. Thermodynamic structure of supercritical LOX–GH2 diffusion flames. Combust Flame 2018;196:364–76.
[14] Qiao Z, Lv Y, Hickey J-P. Single-phase instability of intermediate flamelet states in high-pressure combustion. Fuel 2021;288:119736.
[15] Poschner M, Pfitzner M. Real gas CFD simulation of supercritical H2-LOX in the MASCOTTE single injector combustor using a commercial CFD code. In: 46th AIAA Aerospace Sciences Meeting and Exhibit; 2008. p. 952.
[16] Cutrone L, Palma PD, Pascazio G, Napolitano M. A RANS flamelet–progress-variable method for computing reacting flows of real-gas mixtures. Comput Fluid 2010;39(3):485–98.
[17] Kim T, Kim Y, Kim S-K. Real-fluid flamelet modeling for gaseous hydrogen/cryogenic liquid oxygen jet flames at supercritical pressure. J Supercrit Fluids 2011;58(2):254–62.
[18] Perakis N, Haidn OJ, Eiringhaus D, Rahn D, Zhang S, Daimon Y, Karl S, Horchler T. Qualitative and quantitative comparison of RANS simulation results for a 7-element GOX/GCH4 rocket combustor. In: 2018 Joint Propulsion Conference; 2018. p. 4556.

[19] Schmitt T, Méry Y, Boileau M, Candel S. Large-eddy simulation of oxygen/methane flames under transcritical conditions. Proc Combust Inst 2011;33(1):1383–90.
[20] Hickey J-P, Ma PC, Ihme M, Thakur S. Large eddy simulation of shear coaxial rocket injector: real fluid effects. AIAA Pap 2013:4071.
[21] Petit X, Ribert G, Domingo P. Framework for real-gas compressible reacting flows with tabulated thermochemistry. J Supercrit Fluids 2015;101:1–16.
[22] Huo H, Yang V. Large-eddy simulation of supercritical combustion: model validation against gaseous H2–O2 injector. J Propul Power 2017;33(5):1272–84.
[23] Guven U, Ribert G. Impact of non-ideal transport modeling on supercritical flow simulation. Proc Combust Inst 2019;37(3):3255–62.
[24] Schmitt T. Large-eddy simulations of the Mascotte test cases operating at supercritical pressure, Flow. Turbul Combust 2020;105(1):159–89.
[25] Candel S, Herding G, Synder R, Scouflaire P, Rolon C, Vingert L, Habiballah M, Grisch F, Péalat M, Bouchardy P, et al. Experimental investigation of shear coaxial cryogenic jet flames. J Propul Power 1998;14(5):826–34.
[26] Haidn O, Habiballah M. Research on high pressure cryogenic combustion. Aero Sci Technol 2003;7(6):473–91.
[27] Habiballah M, Orain M, Grisch F, Vingert L, Gicquel P. Experimental studies of high-pressure cryogenic flames on the mascotte facility. Combust Sci Technol 2006;178(1–3):101–28.
[28] Candel S, Juniper M, Singla G, Scouflaire P, Rolon C. Structure and dynamics of cryogenic flames at supercritical pressure. Combust Sci Technol 2006;178(1–3):161–92.
[29] Mayer W, Tamura H. Propellant injection in a liquid oxygen/gaseous hydrogen rocket engine. J Propul Power 1996;12(6):1137–47.
[30] Mayer W, Schik A, Schaffler M, Tamura H. Injection and mixing processes in high-pressure liquid oxygen/gaseous hydrogen rocket combustors. J Propul Power 2000;16(5):823–8.
[31] Juniper M, Tripathi A, Scouflaire P, Rolon J-C, Candel S. Structure of cryogenic flames at elevated pressures. Proc Combust Inst 2000;28(1):1103–9.
[32] Armbruster W, Hardi J, Oschwald M. Impact of shear-coaxial injector hydrodynamics on high-frequency combustion instabilities in a representative cryogenic rocket engine. Int J Spray Combust Dyn 2022;14(1–2):118–30.
[33] Bhattacharya A, Basu S. An investigation into the heat release and emissions from counterflow diffusion flames of methane/dimethyl ether/hydrogen blends in air. Int J Hydrogen Energy 2019;44(39):22328–46.
[34] Juniper M, Darabiha N, Candel S. The extinction limits of a hydrogen counterflow diffusion flame above liquid oxygen. Combust Flame 2003;135(1–2):87–96.
[35] Traxinger C, Zips J, Pfitzner M. Single-phase instability in non-premixed flames under liquid rocket engine relevant conditions. J Propul Power 2019;35(4):675–89.
[36] Yao MX, Hickey J-P, Ma PC, Ihme M. Molecular diffusion and phase stability in high-pressure combustion. Combust Flame 2019;210:302–14.
[37] Tudisco P, Menon S. Numerical investigations of phase-separation during multi-component mixing at super-critical conditions. Flow, Turbul Combust 2020;104(2):693–724.
[38] Vance FH, de Goey P, van Oijen JA. The effect of thermal diffusion on stabilization of premixed flames. Combust Flame 2020;216:45–57.
[39] Stephen RT. An introduction to combustion: concepts and applications. McGrw-Hill Companies, Inc; 2000.
[40] Law CK. Combustion physics. Cambridge University Press; 2010.
[41] Pitsch H. Flamemaster: a C++ computer program for 0D combustion and 1D laminar flame calculations. 1998. Cited in 81.
[42] Peng D-Y, Robinson DB. A new two-constant equation of state. Ind Eng Chem Res 1976;15(1):59–64.
[43] Harstad KG, Miller RS, Bellan J. Efficient high-pressure state equations. AIChE J 1997;43(6):1605–10.
[44] Meng H, Yang V. A unified treatment of general fluid thermodynamics and its application to a preconditioning scheme. J Comput Phys 2003;189(1):277–304.
[45] Elliott JR, Lira CT, Lira CT. Introductory chemical engineering thermodynamics, vol. 668. Upper Saddle River, NJ: Prentice Hall; 2012.
[46] McBride BJ. Coefficients for calculating thermodynamic and transport properties of individual species, vol. 4513. NASA Langley Research Center; 1993.
[47] Chung TH, Ajlan M, Lee LL, Starling KE. Generalized multiparameter correlation for nonpolar and polar fluid transport properties. Ind Eng Chem Res 1988;27(4):671–9.
[48] Chapman S, Cowling TG. Mathematical theory of non-uniform gases. 3rd ed. Cambridge Press; 1970.
[49] Takahashi S. Preparation of a generalized chart for the diffusion coefficients of gases at high pressures. J Chem Eng Jpn 1975;7(6):417–20.
[50] Burke MP, Chaos M, Ju Y, Dryer FL, Klippenstein SJ. Comprehensive H2/O2 kinetic model for high-pressure combustion. Int J Chem Kinet 2012;44(7):444–74.
[51] Milan PJ, Hickey J-P, Wang X, Yang V. Deep-learning accelerated calculation of real-fluid properties in numerical simulation of complex flowfields. J Comput Phys 2021;444:110567.
[52] Linstrom PJ, Mallard WG. NIST chemistry webbook, NIST standard reference database number 69. Gaithersburg, MD: National Institute of Standards and Technology; 1998. http://webbook.nist.gov/chemistry.
[53] Laurent C, Esclapez L, Maestro D, Staffelbach G, Cuenot B, Selle L, Schmitt T, Duchaine F, Poinsot T. Flame–wall interaction effects on the flame root stabilization mechanisms of a doubly-transcritical LO2/LCH4 cryogenic flame. Proc Combust Inst 2019;37(4):5147–54.
[54] Blanchard S, Cazères Q, Cuenot B. Chemical modeling for methane oxy-combustion in liquid rocket engines. Acta Astronaut 2022;190:98–111.
[55] Sutherland J, Smith P, Chen J. Quantification of differential diffusion in nonpremixed systems. Combust Theor Model 2005;9(2):365–83.
[56] Bell IH, Wronski J, Quoilin S, Lemort V. Pure and pseudo-pure fluid thermophysical property evaluation and the open-source thermophysical property library coolprop. Ind Eng Chem Res 2014;53(6):2498–508.
[57] Michelsen ML. The isothermal flash problem. Part I. Stability. Fluid Phase Equil 1982;9(1):1–19.
[58] Bakhtar F, Young J, White A, Simpson D. Classical nucleation theory and its application to condensing steam flow calculations. Proc IME C J Mech Eng Sci 2005;219(12):1315–33.